ELSEVIER

Advances in Water Resources 24 (2001) 63–72

Advances in Water Resources

www.elsevier.com/locate/advwatres

Numerical modelling of convection dominated transport coupled with density driven flow in porous media

Peter Frolkovič, Hennie De Schepper *

Department of Mathematical Analysis, University of Gent, Galglaan 2, 9000 Gent, Belgium

Received 12 July 1999; received in revised form 7 February 2000; accepted 12 April 2000

Abstract

In this paper, we present a numerical model for a problem of coupled flow and transport in porous media. We use a barycentre based finite volume method (FVM), which, in the case of convection dominated transport, is combined with suitable upwind methods, in order to avoid numerical instabilities. We present some relevant and new numerical results for the Elder problem, which offer a better understanding of mutually non-compatible results in other papers, by showing the dependence of the recirculating patterns on the level of grid refinement and on the numerical scheme, as well as on (numerical) perturbations.

Keywords: Density driven flow; Convection dominated transport; Finite volume methods; Upwind methods; Discrete maximum principle; Elder problem

1. Introduction

When studying flow and transport phenomena in porous media, one may observe that the transported component influences the flow patterns, leading to a *fully* coupled problem of transport and flow. Typically, the varying concentration of the transported species directly affects the fluid density, which can result in flow pattern formation, due to the gravity forces. Such phenomena are usually indicated as density driven flow, [13], or buoyancy induced flow [11].

A motivation for the mathematical problem considered may be the modelling of groundwater flow near salt domes, where the fluid is a mixture of pure water and brine, see [8,12,13,23] or the modelling of an evaporating salt lake, where dense brine overlies a less dense fluid, [26]. However, our paper rather has an academical purpose.

The mathematical model of nonlinear coupled flow and transport is quite involved. Analytical solutions are known for simplified situations only, see [29]. The same holds for the error analysis of well-established numerical schemes. Hence, for more involved situations, numerical methods which preserve known analytical or physical properties are preferable in view of the reliability of the computed solutions. In this paper, we design discretisation schemes which preserve a local mass conservation property, and which moreover lead to physically acceptable values for the unknown concentration of the transported species.

The paper is organized as follows.

In Section 2, we briefly recall the mathematical model.

In Section 3, we introduce so-called vertex centered finite volume methods (FVMs), which preserve a local mass balance. They are related to finite element methods (FEMs), as the finite volume mesh is constructed complementary to a standard, well-chosen finite element mesh – triangular or quadrangular. Here, we restrict ourselves to a 2D-approach, corresponding e.g., to a vertical cross-section of the physical domain. These FVMs were presented first in various applications of flow and transport, see e.g. [24]. More recently, they have also been studied from the theoretical point of view, see [2,10,15,28].

In Section 4, we prove a discrete minimum and maximum property for the numerical solution of the transport equation. This allows us to predict non-physical behaviour of the numerical solution (e.g.,

* Corresponding author. Tel.: +32-9-264-48-97; fax: +32-9-264-49-87; http://cage.rug.ac.be/~hds/nufarg/.

E-mail addresses: pfrolko@cage.rug.ac.be (P. Frolkovič), hds@cage.rug.ac.be (H. De Schepper).

0309-1708/01/$ - see front matter
PII: S0309-1708(00)00025-7

under- and overshooting, non-physical oscillations,...). Such behaviour may occur either due to the approximation of complex (anisotropic, variable) diffusion–dispersion fluxes, or due to the convection dominated character of the transport equation.

In Section 5, we consider the case, where the minimum and maximum principle mentioned above fails, due to convection dominated transport. In this case we propose a class of upwind methods, retaining the idea of a discrete local mass balance. Several advanced types of upwind methods were presented already in [24] and have also been studied theoretically, e.g., in [2,14].

Finally, in Section 6, we present numerical results for the Elder experiment, [6]. Moreover, for this benchmark, we show the advantages of some advanced upwind schemes. Although the Elder problem originates from thermodynamics, it has become a popular benchmark in mass transfer with variable density flow (in particular brine transport, see [1,3,18,19,21,23,30]), due to its complex dynamical behaviour. This example has been chosen amongst others, as the computations offer clear insight into the effectiveness of the numerical schemes.

Compared to existing results in the literature, see [2,9,14,24], the main contribution of this paper concerns the following aspects. We extend the results on the discrete minimum and maximum principle to the general case of nonlinear transient coupled flow and transport, using FVMs based on both triangular and quadrangular meshes. Moreover, we consider the more complex case of anisotropic diffusive–dispersive transport, and we derive a general class of upwind methods in this context. Furthermore, our results for the Elder problem are new. They allow for a better judgment of some mutually non-compatible numerical results and conclusions in different papers, see [6,19,21,23,30].

2. Mathematical model

The mathematical model below describes a miscible displacement of salt water (brine) and fresh water, constituting a "binary fluid mixture", e.g. [4,12,13, 21,23,30]. The unknown mass fraction of brine is denoted by $c = c(t,x)$, where $x \in \Omega \subset \mathbb{R}^2$ and $t \geqslant 0$. The variability of the fluid density is expressed through a (nonlinear) equation of state, $\rho = \rho(c) \geqslant \rho_w$, ρ_w denoting the density of fresh water. The dependence of ρ on the fluid temperature or on the compressibility of the fluid is neglected. The flow and transport equations are

$$\phi\, \partial_t \rho(c) + \nabla \cdot (\rho(c)\mathbf{v}) = \rho(C)Q, \tag{1}$$

$$\phi\, \partial_t (\rho(c)c) + \nabla \cdot \rho(c)(c\mathbf{v} - D\nabla c) = \rho(C)CQ. \tag{2}$$

Here, $\phi = \phi(x)$ is the porosity of the soil, $Q = Q(t,x)$ describes external sources and sinks, C either denotes a given (injected) mass fraction of externally supplied brine ($Q > 0$), or $C \equiv c$ for extraction wells ($Q < 0$), and $D = D(x,\mathbf{v})$ is the diffusion–dispersion matrix, see e.g. [4]. Finally, $\mathbf{v}$ is the mass averaged velocity, given by Darcy's law, see e.g. [4],

$$\mathbf{v} = -\frac{k}{\mu(c)}(\nabla p - \rho(c)\mathbf{g}), \tag{3}$$

where $p = p(t,x)$ stands for the unknown fluid pressure. Through (3), Eqs. (1) and (2) form a (nonlinear and fully coupled) system for two unknown functions c and p. Further data, entering $\mathbf{v}$, are the fluid viscosity $\mu = \mu(c)$, the permeability matrix $k = k(x)$ and the gravity vector $\mathbf{g}$.

Suitable initial and boundary conditions (ICs and BCs), see [4,8,12,20,21] must accompany (1) and (2). For the sake of simplicity we will only consider standard Dirichlet and (homogeneous) Neumann BCs. Formally, an IC needs to be supplied for c only. However, from the numerical point of view, a reasonable initial pressure distribution can be useful, see e.g. [8,21].

3. Finite volume methods

In this section, we describe the vertex centered finite volume discretisation of the system (1)–(3). To fix the ideas, let Ω be polygonal. We consider a triangulation $\mathscr{T}$ of Ω, in the sense of [5], consisting of triangular and/or quadrangular elements T^e, $e = 1,\ldots,E$ which is used to define a FE-mesh. The corresponding set of nodes, denoted by x_i, $i = 1,\ldots,N$, consists of the vertices of all elements T^e in $\mathscr{T}$. Further, we consider time points $0 = t_0 < t_1 < \cdots$ and we denote $\tau_m = t_m - t_{m-1}$, $m \in \mathbb{N}_0$.

In general, the data functions in Eqs. (1)–(3) will show a number of discontinuities in Ω. To incorporate this in our numerical model, we assume that $\mathscr{T}$ is constructed such that the data are continuous inside each element.

At any time point t_m, we consider the functions

$$\tilde{c} \equiv \tilde{c}^m(x) = \sum_{i=1}^{N} c_i^m N_i(x),$$

$$\tilde{p} \equiv \tilde{p}^m(x) = \sum_{i=1}^{N} p_i^m N_i(x), \quad x \in \Omega, \tag{4}$$

where N_i, $i = 1,\ldots,N$, are the usual, globally continuous finite element basis functions, defined piecewise and obeying $N_i(x_j) = \delta_{ij}$, $j = 1,\ldots,N$. The function ∇N_i is well-defined per element. In (4), $\{c_i^m, p_i^m\}_{i=1}^N$ are unknown discrete variables, approximating the nodal values $c(t_m,x_i)$ and $p(t_m,x_i)$, respectively.

We set up an algebraic system for $\{c_i^m, p_i^m\}_{i=1}^N$, which can be solved sequentially for $m = 1,2,\ldots$, the values c_i^0 (and preferably also p_i^0) being determined by ICs. To

this end, we first introduce a local mass balance in integral form, starting from (2), i.e.,

$$\int_V \phi\rho(c(t))c(t)\,\mathrm{d}x - \int_V \phi\rho(c(\hat{t}))c(\hat{t})\,\mathrm{d}x = -\int_{\hat{t}}^{t}\int_{\partial V} \rho(c)\mathbf{n}\cdot(c\mathbf{v} - D\nabla c)\,\mathrm{d}\gamma\,\mathrm{d}t + \int_{\hat{t}}^{t}\int_V \rho(C)CQ\,\mathrm{d}x\,\mathrm{d}t \tag{5}$$

and similarly for (1). Here, $V \subset \Omega$ and $(\hat{t}, t)$ is an arbitrary time interval.

Next, to derive vertex centered FVMs, we introduce a dual mesh, by constructing the finite volume $V_i \neq \emptyset$ for each vertex x_i. Here, we deal with barycenter based finite volumes, but other types of vertex centered finite volumes may be considered as well, see [2,9,14,16]. We define the finite volume V_i as the polygonal, bounded by Γ_i (when $x_i \notin \partial\Omega$), or by $\Gamma_i \cup \Gamma_i^0$ (when $x_i \in \partial\Omega$), with $\Gamma_i = \cup_{e\in\Lambda_i} \cup_{j\in\Lambda_i^e} \Gamma_{ij}^e$ and $\Gamma_i^0 = \cup_{j\in\Lambda_i^0} \Gamma_{ij}^0$. Here, Λ_i is the set of all indices e, such that $x_i \in \partial T^e$; when $e \in \Lambda_i$, Λ_i^e is the set of all indices j, such that x_i and x_j are neighbouring nodes on ∂T^e, and finally, for $x_i \in \partial\Omega$, Λ_i^0 is the set of all indices j such that x_i and x_j are neighbouring nodes on $\partial\Omega$. Further, Γ_{ij}^e is the line segment, connecting the barycenter x^e of the element T^e with the midpoint x_{ij} of $\overline{x_i x_{ij}}$, while Γ_{ij}^0 stands for the line segment $\overline{x_i x_{ij}}$, when x_i and $x_j \in \partial\Omega$. An illustration of the notations is given by Fig. 1.

We consider (5) and its analogon for the flow equation for $V = V_i$ and for the generic time interval (t_{m-1}, t_m). To simplify the treatment of the BCs, we assume that $\{c_i^m, p_i^m\}_{i=I+1}^N$ are prescribed by Dirichlet BCs, which allows us to consider only $i = 1,\ldots,I$. Moreover, at the remaining part of $\partial\Omega$ we impose zero flux BCs, causing eventual integrals over Γ_i^0 to drop out. For a more involved treatment of BCs, we refer to [8,9].

Furthermore, we approximate c and p by (4) and we apply suitable quadrature rules, deliberately chosen as follows: for time integrals we use an implicit Euler scheme, by evaluation of the integrand at $t = t_m$; for integrals over $V_i^e \equiv V_i \cap T^e$, we resort to a mass lumping scheme, by evaluation of the integrand at $x = x_i$; finally, line integrals over Γ_{ij}^e will be approximated by evaluation of the integrand at a well-chosen point $x_{ij}^e \equiv x_{ji}^e \in \Gamma_{ij}^e$, taken to be x_{ij} for the convective part. Other quadrature rules could also be considered, see [14] for e.g., the Crank–Nicholson scheme or the consistent mass scheme.

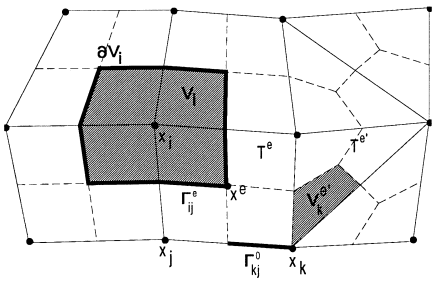

Fig. 1. Notations for finite volume meshes.

In order to write the resulting algebraic system in a transparent form, some further notations must be introduced. Eventual discontinuities of the space dependent coefficient functions between two elements are taken into account by the notation f_i^e or f_{ij}^e for the extension of a function f on T^e to $x_i \in \partial T^e$ or to $x_{ij} \in \partial T^e$, respectively. Moreover for time dependent data we omit the upper index m (e.g., $c_i \equiv c_i^m$) and we write $c_{ij} \equiv \tilde{c}^m(x_{ij})$, $c_{ij}^e \equiv \tilde{c}^m(x_{ij}^e)$, $\nabla c_{ij}^e \equiv \nabla\tilde{c}^m(x_{ij}^e)$ and analogously for p. Finally, by $|V_i^e|$ and by $|\Gamma_{ij}^e|$ we, respectively, denote the area of V_i^e and the length of Γ_{ij}^e. We arrive at the system

$$\sum_{e\in\Lambda_i} |V_i^e|\phi_i^e\rho(c_i) + \tau_m \sum_{e\in\Lambda_i}\sum_{j\in\Lambda_i^e} |\Gamma_{ij}^e|\rho(c_{ij})\mathbf{n}_{ij}^e\cdot\mathbf{v}_{ij}^e = \sum_{e\in\Lambda_i} |V_i^e|\big(\phi_i^e\rho\big(c_i^{m-1}\big) + \tau_m\,\rho(C_i^e)Q_i^e\big), \quad i = 1,\ldots,I \tag{6}$$

and

$$\sum_{e\in\Lambda_i} |V_i^e|\phi_i^e\rho(c_i)c_i + \tau_m \sum_{e\in\Lambda_i}\sum_{j\in\Lambda_i^e} |\Gamma_{ij}^e|\mathbf{n}_{ij}^e \cdot \Big(\rho(c_{ij})c_{ij}\mathbf{v}_{ij}^e - \rho(c_{ij}^e)D_{ij}^e\nabla c_{ij}^e\Big) = \sum_{e\in\Lambda_i} |V_i^e|\big(\phi_i^e\rho\big(c_i^{m-1}\big)c_i^{m-1} + \tau_m\,\rho(C_i^e)C_i^eQ_i^e\big), \quad i = 1,\ldots,I. \tag{7}$$

Here, $\mathbf{n}_{ij}^e$ is the unit normal vector on Γ_{ij}^e, pointing from V_i to V_j. If no special approximation of $\mathbf{v}$ is used (see [7,17,30] for the consistent velocity approximation), we simply put

$$\mathbf{v}_{ij}^e = -\frac{k_{ij}^e}{\mu(c_{ij})}\Big(\nabla p_{ij}^e - \rho(c_{ij})\mathbf{g}\Big). \tag{8}$$

Notice that equations can be assembled elementwise, as in FEMs, the resulting algebraic system being nonlinear, coupled and sparse.

Remark 1. Eqs. (6) and (7) can be interpreted as discrete local mass conservation properties in the finite volume V_i, during the time interval (t_{m-1}, t_m). These mass balances also hold in the union of two adjacent finite volumes, leading, by continuation, to discrete conservation laws in the whole domain. When adapting the grid between subsequent time points, see [18], we should retain these mass balances. In particular,

$$\sum_{i=1}^N \rho(c_i)\sum_{e\in\Lambda_i} |V_i^e|\phi_i^e \quad \text{and} \quad \sum_{i=1}^N \rho(c_i)c_i\sum_{e\in\Lambda_i} |V_i^e|\phi_i^e,$$

should be preserved, as they represent in a discrete sense the total mass of fluid, respectively, of salt in Ω at $t = t_m$.

We also give an equivalent form of (7), which will help us to study the discrete minimum and maximum principle and to introduce upwind methods. Invoking (6), (7) may be rewritten in the form

$$\sum_{e\in\Lambda_i}|V_i^e|\phi_i^e\rho\left(c_i^{m-1}\right)\left(c_i-c_i^{m-1}\right)+\tau_m\sum_{e\in\Lambda_i}\sum_{j\in\Lambda_i^e}|\Gamma_{ij}^e|\mathbf{n}_{ij}^e \cdot\left(\rho(c_{ij})\left(\hat{c}_{ij}^e-c_i\right)\mathbf{v}_{ij}^e-\rho(c_{ij}^e)D_{ij}^e\nabla c_{ij}^e\right)+\tau_m\sum_{e\in\Lambda_i}|V_i^e|\rho(C_i^e)\left(c_i-C_i^e\right)Q_i^e=0,\quad i=1,\ldots,I. \tag{9}$$

Above, we formally introduced the notation

$$\hat{c}_{ij}^e=c_i+\hat{\beta}_{ij}^e(c_j-c_i),\quad j\in\Lambda_i^e,\ \ e\in\Lambda_i, \tag{10}$$

where $\hat{\beta}_{ji}^e=\hat{\beta}_{ij}^e=1/2$, implying that $\hat{c}_{ij}^e\equiv c_{ij}$. Hence, (7) and (9) are equivalent. In Sections 5 and 6, this will be referred to as the *no upwind* scheme.

Let $k\in\Lambda^e$ when $x_k\in T^e$. Introducing the scalars

$$\lambda_{ik}^e=\frac{1}{\rho(c_{ik})}\sum_{j\in\Lambda_i^e}|\Gamma_{ij}^e|\rho(c_{ij}^e)\mathbf{n}_{ij}^e\cdot D_{ij}^e\nabla N_k(x_{ij}^e),\quad k\in\Lambda^e\setminus\{i\}, \tag{11}$$

$$\gamma_{ij}^e=|\Gamma_{ij}^e|\mathbf{n}_{ij}^e\cdot\mathbf{v}_{ij}^e,\quad j\in\Lambda_i^e, \tag{12}$$

which characterise the diffusive–dispersive and the convective part of the numerical fluxes, respectively, (9) can be rewritten as

$$\rho\left(c_i^{m-1}\right)\sum_{e\in\Lambda_i}|V_i^e|\phi_i^e\left(c_i-c_i^{m-1}\right)+\tau_m\sum_{e\in\Lambda_i}\sum_{k\in\Lambda_e\setminus\{i\}}\rho(c_{ik})\left(\lambda_{ik}^e-\hat{\beta}_{ik}^e\gamma_{ik}^e\right)(c_i-c_k)+\tau_m\sum_{e\in\Lambda_i}|V_i^e|\rho(C_i^e)Q_i^e\left(c_i-C_i^e\right)=0,\quad i=1,\ldots,I, \tag{13}$$

where we formally take $\hat{\beta}_{ik}^e=1/2$, and $\gamma_{ik}^e=0$ when $k\in\Lambda^e\setminus\Lambda_i^e,\ k\neq i$.

Remark 2. Eqs. (6) and (13) form a system of nonlinear algebraic equations, to be solved by some nonlinear iterative solver, where in each iteration a linearisation of the nonlinear algebraic system has to be provided. For our numerical simulations we choose a fully coupled, nonlinear solver of Newton type. All derivatives in the Jacobi matrix with respect to the unknown discrete variables are computed analytically and no simplifications or decoupling techniques like Pickard iterations are used: see e.g. [25].

4. Discrete minimum and maximum principle

Physically, the range of values for the concentration of the transported species should be bounded – above and below – by extreme values of some given data in the mathematical model. Such a minimum and maximum principle has been proved for the analytical solution of a linear transport equation, where ρ and μ are not dependent on c, see e.g. [27]. Moreover for an appropriate numerical discretisation scheme, also a discrete minimum and maximum principle holds, under some assumptions, see [2,14]. Here, we formulate similar results for nonlinear, coupled flow and transport. For triangular elements and isotropic diffusion without dispersion this was studied in [9]. In this paper, we allow for the more general finite elements considered above, as well as for a general diffusion–dispersion matrix. Moreover, we derive upwind schemes in this general context: cf. Section 5.

In the following two remarks we first discuss some features of λ_{ik}^e, corresponding to particular choices of the quadrature nodes x_{ij}^e, which appear in (11), for the approximation of the diffusive–dispersive fluxes.

Remark 3. As for the approximation of the convective term, we can choose $x_{ij}^e=x_{ij}$. Here, in general, $\lambda_{ik}^e\neq\lambda_{ki}^e$ and, moreover, we cannot judge the sign of λ_{ik}^e. However, for the isotropic case (i.e., $D\equiv\phi dI$), with a grid consisting either of equilateral triangles or of rectangles, we obtain

$$\lambda_{ik}^e=\lambda_{ki}^e=\frac{|\,\Gamma_{ik}^e\,|}{|\,x_i-x_k\,|}\phi_{ik}^e\,d_{ik}^e>0,\quad k\in\Lambda_i^e \tag{14}$$

and zero otherwise, where $d_{ik}^e=d(x_{ik}^e)$: see e.g. [2,14].

Remark 4. We may also choose $x_{ij}^e=x^e$. Then, we get

$$\lambda_{ik}^e=\frac{\rho(c^e)}{\rho(c_{ik})}\left(\sum_{j\in\Lambda_i^e}|\,\Gamma_{ij}^e\,|\,\mathbf{n}_{ij}^e\right)\cdot D^e\nabla N_k(x^e),\quad k\in\Lambda^e\setminus\{i\}.$$

If T^e is a rectangle or a triangle then we obtain that $\lambda_{ik}^e=\lambda_{ki}^e$ (cf. [15] for the case of a triangle). Moreover for the isotropic case and when all angles of the triangular element T^e do not exceed $\pi/2$, we also have $\lambda_{ik}^e\geqslant 0$: see [2,14]. Again, in general, no conclusion concerning the sign of λ_{ik}^e is possible.

Below, the form (13) of the discrete transport equation is the starting point for our considerations.

Theorem 5. *Let* $\{c_i,\ i=1,\ldots,N\}$ *fulfill* (13). *Denote* $c_{i_{\min}}=\min_{i=1,\ldots,\hat{I}}\{c_i\}$ *and* $c_{i_{\max}}=\max_{i=1,\ldots,\hat{I}}\{c_i\}$, *where* $1\leqslant\hat{I}\leqslant I$. *Furthermore, suppose that for* $i=i_{\min}$ *and* $i=i_{\max}$ *we have*

$$\lambda_{ik}^e\geqslant\hat{\beta}_{ik}^e\gamma_{ik}^e\quad\text{for } e\in\Lambda_i,\ \ k\in\Lambda^e\setminus\{i\}. \tag{15}$$

Then,

$$c_{i_{\min}} \geqslant \min\{\min\{c_j \mid j > \hat{I},\ j \in \Lambda^e,\ e \in \Lambda_{i_{\min}}\},$$
$$c^{m-1}_{i_{\min}}, \min\{C^e_{i_{\min}} \mid e \in \Lambda_{i_{\min}}\}\},$$
$$c_{i_{\max}} \leqslant \max\{\max\{c_j \mid j > \hat{I},\ j \in \Lambda^e,\ e \in \Lambda_{i_{\max}}\},$$
$$c^{m-1}_{i_{\max}}, \max\{C^e_{i_{\max}} \mid e \in \Lambda_{i_{\max}}\}\}.$$

Proof. Consider (13) for $i = i_{\min}$ and $i = i_{\max}$. It suffices to notice that all coefficients in this equation are non-negative and some are strictly positive. □

The theorem above allows us to study the numerical solution locally, for any subset of $\{c_i \mid i = 1, \ldots, I\}$, including the case of a single equation. In particular, when (15) is not fulfilled, this theorem is no longer valid and non-physical behaviour of the numerical solution could be observed. This may occur in the following two situations. First, if $\lambda^e_{ik} < 0$ in (15), the condition fails when $\gamma^e_{ik} \geqslant 0$. In other words, (15) can be violated, even in the case of *zero* convection ($\gamma^e_{ik} = 0$), due to the approximation of the diffusive–dispersive fluxes. However, also when $\lambda^e_{ik} \geqslant 0$, (15) can fail, viz., when $\gamma^e_{ik}/\lambda^e_{ik} > 1/\hat{\beta}^e_{ik} = 2$. *Mathematically*, this corresponds to the numerical representation of so-called convection dominated transport, dealt with in Section 5.

5. Upwind algorithms

The term convection dominated transport is used when the ratio of the relative contribution of convection versus diffusion–dispersion to the solute transport is larger then one. For the discrete transport equation (13), the relation between the effectiveness of discrete mass transport due to convection and to diffusion–dispersion can be expressed in a convenient way by the (dimensionless) grid Peclet numbers,

$$P^e_{ik} = \frac{\gamma^e_{ik}}{\lambda^e_{ik}},\ \text{when } \lambda^e_{ik} \neq 0 \quad \text{for } e \in \Lambda_i,\ k \in \Lambda^e \setminus \{i\}. \tag{16}$$

Hence, when $\lambda^e_{ik} > 0$, Eq. (15) can be reformulated as

$$P^e_{ik} \leqslant 2, \quad e \in \Lambda_i,\ k \in \Lambda^e \setminus \{i\}. \tag{17}$$

If (17) fails, the minimum and maximum principle above does not hold, and we can expect instabilities (non-physical oscillations) in the numerical simulations. In order to avoid the restriction (17), we resort to other methods when dealing mathematically with the case of a convection dominated discrete transport equation. We present so-called upwind methods, which retain the concept of local mass conservation.

The idea is to modify (13), by no longer taking $\hat{\beta}^e_{ij} = 1/2$. Consequently, we are not dealing anymore with a direct approximation of the exact mass balance (5), in which c and p have been replaced by $\tilde{c}$ and $\tilde{p}$, (4) and to which numerical quadrature has been applied. Yet, we can interpret upwind methods as the replacement of $\tilde{c}$ by another approximation of c, which is more suitable for the convective–diffusive fluxes.

We proceed as follows: see [2,24]. Define, for some function $u(s),\ s \in (0,1)$,

$$J^e_{ij} \equiv J^e_{ij}(u(s)) = \gamma^e_{ij}(u(s) - c_i) - \lambda^e_{ij}\,\partial_s u(s),$$
$$i = 1, \ldots, I,\ \ e \in \Lambda_i,\ \ j \in \Lambda^e_i.$$

For $\tilde{u}(s) \equiv \tilde{c}(x(s))$, with $x(s) \equiv x_i + (x_j - x_i)s$, we have $\tilde{u}(s) = c_i + (c_j - c_i)s$. The corresponding values $J^e_{ij}(\tilde{u}(1/2))$ appear exactly in (13). Moreover, in the situation of Remark 3 we have

$$|\,\Gamma^e_{ij}\,|\,\mathbf{n}^e_{ij} \cdot \left(\mathbf{v}^e_{ij}(c(t_m, x(s)) - c_i) - d^e_{ij}\nabla c(t_m, x(s))\right)$$
$$= J^e_{ij}(c(t_m, x(s))).$$

We aim at replacing the function $\tilde{u}$, approximating $c(t_m, x(s))$, by a more appropriate interpolation profile $\hat{u}$, leading to a constant value of $J^e_{ij}(\hat{u}(s))$ for $s \in (0,1)$. This function is found as the exact solution of the equation

$$\partial_s J^e_{ij}(u(s)) = 0,\ \ s \in (0,1), \quad \text{with } u(0) = c_i,\ \ u(1) = c_j. \tag{18}$$

For $\lambda^e_{ij} = 0$, i.e., the hyperbolic case, only the BC at the inflow boundary is imposed, i.e., $u(0) = c_i$ for $\gamma^e_{ij} > 0$ or $u(1) = c_j$ for $\gamma^e_{ij} < 0$. Consequently, the function $\hat{u}$ is given by

$$\hat{u} \equiv \hat{u}(s)$$
$$= \begin{cases} c_i + (c_j - c_i)\frac{\exp(P^e_{ij}s)-1}{\exp(P^e_{ij})-1}, & \lambda^e_{ij} \neq 0, \quad \gamma^e_{ij} \neq 0, \\ c_i + (c_j - c_i)s, & \lambda^e_{ij} \neq 0, \quad \gamma^e_{ij} = 0, \\ c_i, & \lambda^e_{ij} = 0, \quad \gamma^e_{ij} > 0, \\ c_j, & \lambda^e_{ij} = 0, \quad \gamma^e_{ij} < 0. \end{cases} \tag{19}$$

Next, we define $\hat{J}^e_{ij} = (\lambda^e_{ij} - \beta^e_{ij}\gamma^e_{ij})(c_i - c_j)$, where

$$\beta^e_{ij} = \begin{cases} \frac{1}{P^e_{ij}} - \frac{1}{\exp(P^e_{ij})-1}, & \lambda^e_{ij} > 0, \quad \gamma^e_{ij} \neq 0, \\ 0, & \lambda^e_{ij} \leqslant 0, \quad \gamma^e_{ij} > 0, \\ 1, & \lambda^e_{ij} \leqslant 0, \quad \gamma^e_{ij} < 0. \end{cases} \tag{20}$$

Note that if $\lambda^e_{ij} \geqslant 0$, then $\hat{J}^e_{ij} \equiv J^e_{ij}(\hat{u})$. Moreover, we do not need to define β^e_{ij} when $\gamma^e_{ij} = 0$. When $\lambda^e_{ij} < 0$, to avoid so-called *downwind* schemes, the value of β^e_{ij} corresponds to the case $\lambda^e_{ij} = 0$ in (19). If $\lambda^e_{ij} = \lambda^e_{ji}$, we can easily show that $\beta^e_{ji} = 1 - \beta^e_{ij}$, as $P^e_{ji} = -P^e_{ij}$. In general, we *define* $\hat{\beta}^e_{ij}$, entering (10), by

$$\hat{\beta}^e_{ij} = \beta^e_{ij} \ \text{ for } \gamma^e_{ij} > 0 \quad \text{and} \quad \hat{\beta}^e_{ij} = 1 - \hat{\beta}^e_{ji} \ \text{ for } \gamma^e_{ij} < 0. \tag{21}$$

As $\gamma^e_{ij} = -\gamma^e_{ji}$, this definition is consistent. Together with (20) it defines the so-called *exponential upwind* scheme. Moreover, from (10), we have that $\hat{c}^e_{ij} \equiv \hat{c}^e_{ji}$ and hence the global discrete mass conservation property is preserved.

Using (21) in the discrete transport equation (13), (15) is seen to be fulfilled for $\lambda_{ij}^e \geqslant 0$. Hence, in this case the discrete minimum and maximum principle is ensured, even for convection dominated transport. The only drawback of the scheme (20) may be the expensive evaluation of the exponential function. To avoid this, other upwind schemes are considered, which are based on a suitable modification of the exponential interpolation profile (19), see [2,24] for details. The simplest example is the *full upwind scheme*, where (20) is replaced by

$$\beta_{ij}^e = 0 \text{ for } \gamma_{ij}^e > 0 \quad \text{and} \quad \beta_{ij}^e = 1 \text{ for } \gamma_{ij}^e < 0. \tag{22}$$

Notice that, for $\lambda_{ij}^e \leqslant 0$, (22) appears in (20). Another popular method is the *partial upwind* (or "hybrid") scheme: see [14,24]. Here (20) is replaced by

$$\beta_{ij}^e = \begin{cases} \frac{1}{2}, & \lambda_{ij}^e > 0, \quad -2 \leqslant P_{ij}^e \leqslant 2, \\ \frac{1}{P_{ij}^e}, & \lambda_{ij}^e > 0, \quad P_{ij}^e > 2, \\ 1 + \frac{1}{P_{ij}^e}, & \lambda_{ij}^e > 0, \quad P_{ij}^e < -2, \\ 0, & \lambda_{ij}^e \leqslant 0, \quad \gamma_{ij}^e > 0, \\ 1, & \lambda_{ij}^e \leqslant 0, \quad \gamma_{ij}^e < 0. \end{cases} \tag{23}$$

Eq. (23) constitutes the smallest modification of (13), required to fulfill (15). In fact for $-2 \leqslant P_{ij}^e \leqslant 2$, no upwind is applied in (23).

For a comparison of the schemes based on (20), (22) and (23), we refer to Fig. 2 below, where the dependence of β_{ij}^e on $P_{ij}^e = \gamma_{ij}^e$ (with $\lambda_{ij}^e \equiv 1$) is shown. From Fig. 2, it is clear that visible differences between the exponential and the partial upwind scheme only occur for $|P_{ij}^e| < 6$, while the full upwind scheme differs significantly from the others for $|P_{ij}^e| < 15$.

Finally, we note that the exponential and the partial upwind scheme depend on the discrete unknowns through $\beta_{ik}^e = \beta_{ik}^e(P_{ik}^e)$ and $P_{ik}^e = P_{ik}^e(c_i, c_k)$. Hence the linearisation of a nonlinear iterative solver has to take into account the derivatives of β_{ik}^e w.r.t. c_i and c_k. In (20), β_{ik}^e depends smoothly on P_{ik}^e, in contrast to (23), where the first derivative jumps for $P_{ik}^e = \pm 2$.

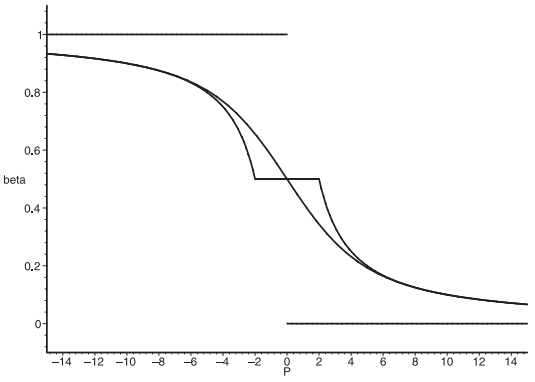

Fig. 2. Comparison of $\beta_{ij}^e(P_{ij}^e)$ for the upwind schemes (20), (22) and (23).

6. Numerical experiments

6.1. Description of the problem

The Elder problem is an example of density driven flow, motivated by experimental measurements of thermally driven convection in porous media, see [6]. A solutal analogue of the thermal convection was defined in [30] and since then the Elder problem became a widely used benchmark for density driven flow simulators, see [1,18,19,21,23], or see [3,13,22] for closely related problems. It describes an instable situation in a closed box, where a dense fluid lies on top of a less dense fluid, see also the modelling of an evaporating salt lake [26]. The complexity of the Elder problem may be presumed from the fact that many authors report qualitatively different numerical results.

In this paper, we use the Elder problem to illustrate the discretisation method outlined above (including upwind methods), and we moreover give an explanation for seemingly incompatible results presented in other papers. Furthermore, we try to provide a reference numerical solution for this problem.

The domain is taken to be rectangular, corresponding to a vertical cross-section of the physical domain. Moreover, by the symmetry of the original problem, it suffices to consider only (the left) half of the rectangle considered in [6,30].

Hence, the computational domain has dimensions 300 m × 150 m, with left bottom corner $(x, y) = (0, 0)$ and right top corner $(x, y) = (300, 150)$.

Initially, $c(0, x, y) = 0$ inside the domain. For the BCs, we strictly follow the model outlined in [30] and implemented by other authors also, although a more appropriate choice could be made, see e.g. [8,20]. For the concentration the BCs are given by the Dirichlet conditions

$$\begin{aligned} c(t, x, 0) &= 0 \qquad \text{for } x \in (0, 300), \ t \geqslant 0, \\ c(t, x, 150) &= 1 \quad \text{for } x \in (150, 300), \ t \geqslant 0 \end{aligned}$$

and by zero flux conditions elsewhere. For the pressure, a zero flux BC is prescribed everywhere, except at the left top corner, where the pressure is supposed to be fixed at the value $p = 0$. Further, we need to specify the data appearing in the mathematical model. First, the equation of state is given by

$$\rho(c) = \left(\frac{1 - c}{\rho_w} + \frac{c}{\rho_b} \right)^{-1},$$

where $\rho_w = 1000$ and $\rho_b = 1200$. Other data are $\phi = 0.1$, $k = 4.845 \times 10^{-13}$, $\mu = 10^{-3}$, $\mathbf{g} = (0, -9.81)$, $D \equiv \phi d I$, with $d = 3.565 \times 10^{-6}$. All values, as well as the specific form of the equation of state, were chosen as in [23].

The discretisation method described in this paper was implemented in the D^{3}F (distributed density driven

flow) package, see [8], itself being based on the numerical library UG (unstructured grids), [3]. In addition, we applied the algorithm of consistent velocity approximation, see e.g. [7]). As we aim at comparing our computations with results from other papers, where no upwind schemes were applied, we have used the partial upwind scheme (23), which only introduces a minimal modification with respect to the no upwind scheme. A discussion of different upwind schemes follows at the end of this section.

The nonlinear algebraic system was solved by a fully coupled, nonlinear iterative solver of Newton type [3], with analytical computations of all derivatives with respect to the unknown discrete variables in the corresponding Jacobi matrix. After each Newton iteration the discrete L_2 norm of the defect (residual) of the system was computed. The iterative process was stopped when the norm of the initial defect (computed from the initial guess) was reduced by a factor 10^{-6} compared to the norm of the last defect. As the convergence for the chosen time step was very good, the iterative procedure required in average only three iterations, after which the norm of the initial defect was reduced in average by a factor 10^{-11}.

6.2. Discretisation method and numerical results

We discretise the domain using a structured, uniform grid with bilinear square elements. Such a grid can be characterised by its level, defined as follows: the grid at the lth level, ($l = 0, 1, 2, \ldots$), consists of 2^{2l+1} identical square elements. The computations were executed at grid level 7: (i.e., with 32 768 elements) and with a uniform time step $\tau = 0.025$ yr. The corresponding numerical results are presented in Fig. 3, where the mass fraction isolines $c = 0.2,\ 0.4,\ 0.6$ and 0.8 are shown, as well as the velocity field $\mathbf{v}$ at chosen points in the domain, at 12 different time points. Grey arrows in the velocity plot indicate that the length of the velocity vector $\mathbf{v}$ was cut beyond some critical value, in order to avoid long arrows in the graphics.

In what follows, we aim at interpreting the results obtained and at comparing them with those presented in [19,21,23].

Due to the initial density difference at the midpoint of the upper boundary, a flow pattern is developed in the form of a recirculation cell. Thus, due to the convective transport, a so-called "finger" of brine appears, accompanied of two recirculation cells, see Fig. 3 for $t = 1$ yr. Next, density differences in the neighbourhood of the first finger cause the development of a second one, see Fig. 3 for $t = 2$ yr. In total, three fingers and a half are developed (7 in the original domain), see Fig. 3 for $t = 2.5$ and $t = 3$ yr. However, meanwhile, mutual interactions cause the merging of two fingers at some time t in the interval (2 yr, 3 yr), as well as in (5 yr, 6 yr), and

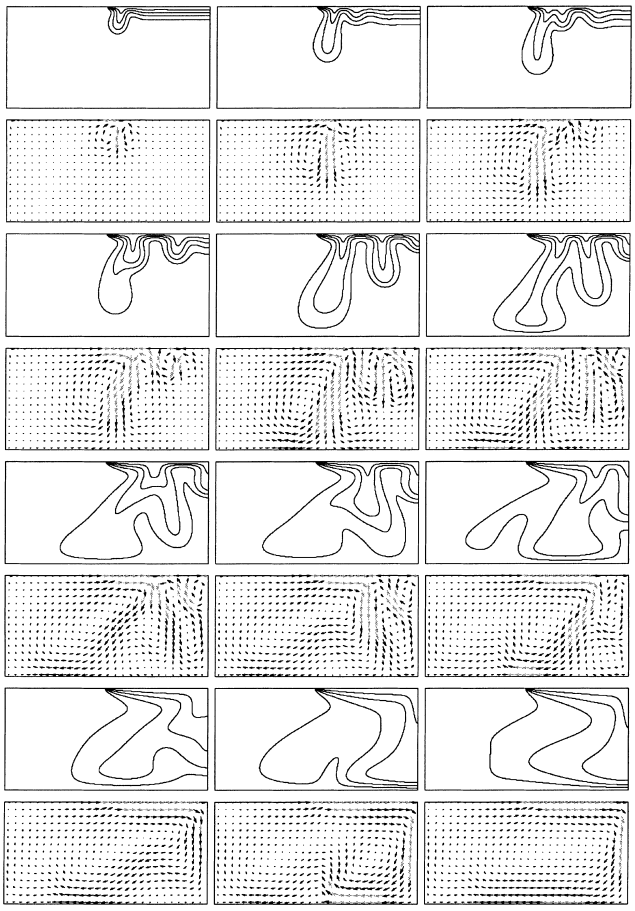

Fig. 3. Results for $t = 1,\ 2,\ 2.5,\ 3,\ 4,\ 5,\ 6,\ 7,\ 10,\ 12,\ 15$ and 20 yr at grid level 7.

finally in (10 yr, 12 yr). As a consequence, when $t > 12$ yr, only a half finger of brine, accompanied of one recirculation cell, can still be observed in Fig. 3. This constitutes a major difference with the results in [19,21,23], where a complete finger of brine is observed for $t = 20$ yr.

To estimate the truncation error from the time discretisation, the "reference" simulations were performed for the time step $\tau = 0.00625$ yr as well. No important visible differences were observed with respect to Fig. 3.

In [23], the computations were executed for grid level 5 and for a non-uniform grid which closely resembles our grid level 6. As the results obtained did not differ significantly for these two "consecutive" grids, the authors concluded to achieve so-called "grid convergence". This conclusion is also quoted by other authors, see e.g. [19,26], but seems to be incorrect. To be able to argue this more profoundly, we have executed some computations on grids of the levels 5 and 6. Here, we have obtained results which are very similar to those presented in [1,19,21,23], as can be seen in Fig. 4.

From these computations, we may also observe that, for $t = 4$ yr, the numerical solutions for the grid levels 6 and 7 are still very resembling, with a minor difference

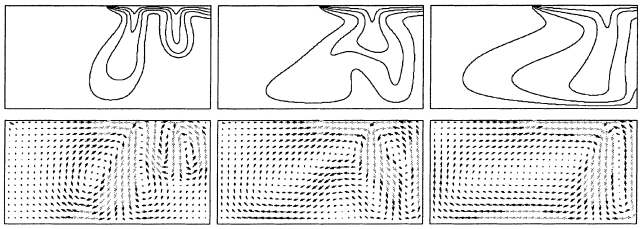

Fig. 4. Results for $t = 4$, 7 and 20 yr at grid level 6.

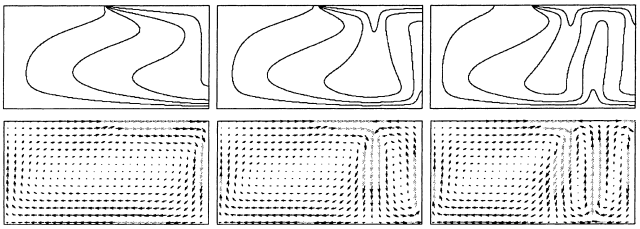

Fig. 6. Different stationary solutions at grid level 7.

concerning the half finger at the top right corner. On the coarser grid, this half finger disappears and the 2 remaining fingers merge at a later time, see $t = 7$ and $t = 20$ yr. For grid level 5 the half finger does not even occur at all for $t = 4$ yr. In general, the finer the grid, the more fingers we may observe at an early stage in the time process. This leads us to the conclusion that the numerical solution at grid level 7 is closer to the exact solution of the Elder problem than the one at grid level 6.

To support this conclusion we resorted to a further, *local* adaptation of the grid, as the computational cost became too high for a uniform refinement up to level 8. In fact, the grid was uniformly refined up to level 6, but the next two grid levels were created by a local refinement procedure, using an a posteriori error estimator, described in [18]. Moreover, this grid refinement (and coarsening) was also applied during the time simulations. The error estimator required to refine all elements near the top boundary side, causing the grid to resemble strongly the one of level 8 at this part of the domain. The numerical results correspond very well to the results at grid level 7: see Fig. 5 for an illustration. Note that the unstructured grid in Fig. 5 not only contains square elements, but also triangles and general quadrangles: see [3,18].

The observation of different "asymptotic" behaviour of the numerical solutions suggests that non-unique stationary solutions exist for the Elder problem. In this context, the notion of a (numerical) stationary solution is used for the transient problem, if the numerical solution no longer changes while continuing with the time process. For the qualitatively very similar problem of Bènard convection, the existence of several stationary solutions has been proved, see [11,13,22]. Here, we have found three different numerical stationary solutions, which differ in the number of fingers and, correspondingly, in the number of recirculation cells. They are presented in Fig. 6 for grid level 7 – however, all three can be observed for various grid levels.

The first solution, shown in the left picture of Fig. 6 was obtained by computing the Elder problem for grid level 7 and for large simulation times. The second one, in the middle, was found by computation of the stationary solution for grid level 6, followed by a uniform refinement of the grid and transient computations for grid level 7. Finally, the third solution, at the right of Fig. 6 was obtained by an analogous strategy, now starting from grid level 4.

Consequently, one may expect very different numerical solutions, when imposing even slightly modified ICs. To illustrate this assertion we consider a very small and local perturbation of the standard ICs. We take e.g., $c(0, 300, 150 - 150/64) = 0.01$, i.e., for one of the vertices of the square element at the upper right corner of the domain, we replace the original zero IC by the value 0.01. The numerical results, obtained for grid level 6 are presented in Fig. 7 at three different times. At $t = 0.5$ yr, one can still observe a strong resemblance with the unperturbed problem, but at $t = 4$ yr, the differences are already very clear. In fact, the solution for the perturbed problem will asymptotically reach the stationary solution, where a half finger of brine occurs, while for the unperturbed problem, the stationary solution shows a complete finger.

Different transient behaviour of the numerical solutions can also be caused by the numerical method itself, see e.g. [22] for the problem of Bènard convection. In particular, when the grid is not aligned according to the sides of the domain, the interpolation of the ICs can cause a perturbation which, eventually, may determine the character of the numerical solution. When however, the refinement of the grid does not affect the character of the perturbation (e.g., by uniform refinement of the initial unstructured grid), one can observe grid convergence of the numerical solution, but the result may differ

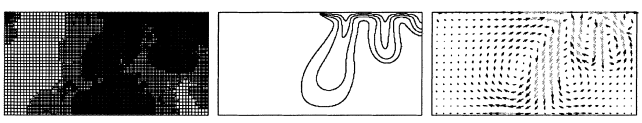

Fig. 5. The locally adaptive grid and the corresponding results for $t = 4$ yr.

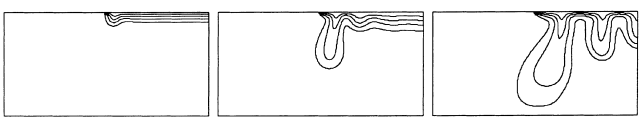

Fig. 7. Results for the perturbed problem at $t = 0.5$, 2 and 4 yr at grid level 6.

from the one presented in Fig. 3. Nevertheless, we may expect the uniform and aligned grid with square elements to be "free" of perturbation.

6.3. Application of various upwind methods

To illustrate the features of the different upwind schemes, for the Elder problem, we compare the cases of the no upwind scheme, the exponential upwind scheme (20) and the full upwind scheme (22).

First, we have executed our computations on a coarse grid of level 4, see Fig. 8 for a comparison of the results at $t = 3.5$ yr. When no upwind is applied, we observe large negative values of c near the middle of the upper boundary. For both upwind methods no negative values of c occur, but only the results based on the exponential scheme resemble the solution with no upwind, while those corresponding to full upwind are significantly different.

In general, the finer the grid, the less apparent the differences between all methods become. In fact for grid level 7 the differences between the no upwind scheme, the exponential scheme (20) and the partial upwind scheme (23) are negligible and not visible in Fig. 3. The negative oscillations in case of no upwind only occur at the early stage of the time process and disappear later on. On the other hand, the full upwind scheme produced the numerical solution analogous to the Fig. 4, even for grid level 7.

As it is clear from the previous subsection, very fine grid refinements are necessary for the Elder problem to resolve the correct development of the numerical solution from the ICs. To explain clearly the advantages of advanced upwind schemes we have computed the Elder problem for different ICs, represented by the results of the full upwind scheme in the right picture of Fig. 8 at $t = 3.5$ yr. Starting from these ICs, grid convergence was reached very quickly. This is confirmed by the following computations. The results for the no upwind scheme are presented in Fig. 9, at $t = 7$ yr for grid levels 4, 5 and 6.

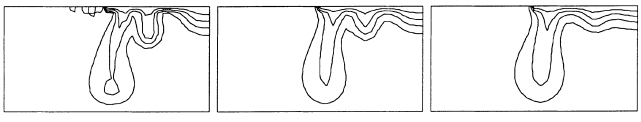

Fig. 8. Comparison of no upwind with the exponential and the full upwind scheme.

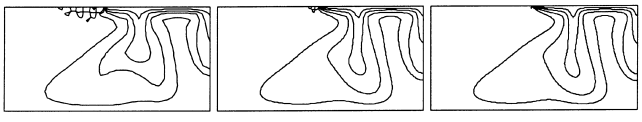

Fig. 9. The no upwind scheme for the grid levels 4, 5 and 6 at $t = 7$ yr.

For the coarse grid level 4 the large negative oscillations develop ($c \approx -1$). They persist in the computations up to grid level 6, but they are getting smaller and they obtain a rather local character. The computations for the exponential upwind scheme are presented in Fig. 10. The comparison of Figs. 9 and 10 suggests that the numerical solutions for grid level 5 for both schemes represent well the exact solution for this special choice of ICs, but only the upwind scheme produces the solution with no non-physical oscillations. For the coarse grid level 4 only the upwind method seems to produce a reasonable numerical approximation of the solution.

As in [13,19,23] one can estimate the "global" Peclet number (also referred to this type of problems as the "Rayleigh" number) by

$$P := \frac{(\rho_b - \rho_w) g k H}{\mu \phi d}, \tag{24}$$

where $g = |\mathbf{g}|$ and H is the height of the domain. For the Elder problem we have $P \approx 400$. This means that for grid level 0 we can estimate the local Peclet numbers by $P^e_{ik} < 400$, for grid level 4 we have $P^e_{ik} < 25$ and finally for grid level 7 we have $P^e_{ik} < 3,125$. From this point of view the behaviour of the no upwind scheme and of the upwind schemes for different grid levels corresponds to our results on the discrete maximum principle.

Finally, we can confirm a slightly better convergence of the iterations for computations with the exponential upwind scheme than with the partial upwind scheme. The convergence was very good in both cases and the difference only became more pronounced for larger time steps.

As in practice, the computational memory is always restricted, advanced upwind methods, like the partial or the exponential upwind scheme, offer several advantages. They produce a physically acceptable numerical solution, without restrictions on the grid Peclet numbers, moreover avoiding excessive grid refinement in the case of convection dominated transport. The full upwind scheme, on the other hand, causes unnecessary large smoothing (or damping) effects and should rather be replaced by more advanced schemes.

It is well-known that upwind methods can impose a grid effect (artificial diffusion) on the numerical solution, if the grid is not aligned to the convective velocity field, see [24]. To reduce such grid effects the method of aligned finite volumes was implemented in D^3F: see [16].

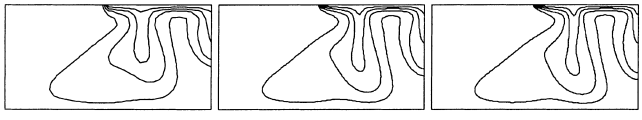

Fig. 10. The exponential upwind scheme for the grid levels 4, 5 and 6 at $t = 7$ yr.

As described in [8,9], upwind methods can successfully be implemented in this context as well.

Acknowledgements

One of the authors (PF) was financially supported by the VEO-project no. 011 VO 697. The authors thank R. Van Keer, coordinator of this project, for stimulating discussions and for his critical reading of the text.

References

[1] Ackerer Ph, Younes A, Mose R. Modelling variable density flow and solute transport in porous media: 1. Numerical model and verification. Transp Porous Media 1999;35(3):345–73.
[2] Angermann L. An introduction to finite volume methods for linear elliptic equations of second order. Institut für Angewandte Mathematik, Universität Erlangen, 1995. Preprint no. 164.
[3] Bastian P, et al. UG – a flexible software toolbox for solving partial differential equations. Comput Visual Sci 1997;1(1):27–40.
[4] Bear J, Verruijt A. Modelling groundwater flow and pollution. Dordrecht: Reidel; 1987.
[5] Ciarlet PG. The finite element methods for elliptic problems. Amsterdam: North-Holland; 1978.
[6] Elder JW. Transient convection in a porous medium. J Fluid Mech 1967;27(3):609–23.
[7] Frolkovič P. Consistent velocity approximation for density driven flow and transport. In: Van Keer R, et al., editors. ACOMEN'98. Maastricht: Shaker; 1998. p. 603–11.
[8] Frolkovič P. Discretization. In: Fein E, editor. d^3f – a simulator for density-driven flow. Gesellschaft fuer Anlagen-und Reaktorsicherheit, Braunschweig, 1999.
[9] Frolkovič P. Maximum principle and local mass balance for numerical solutions of transport equation coupled with variable density flow. Acta Math Univ Com 1998;67(1):137–57.
[10] Fuhrmann J, Langmach H. Stability and existence of solutions of time-implicit finite volume schemes for viscous nonlinear conservation laws. Weierstrass-Inst. für Angew. Analysis und Stochastik, Berlin, 1998. Preprint 437.
[11] Gebhart B, et al. Buoyancy-induced flows and transport. New York: Hemisphere; 1988.
[12] Hassanizadeh SM, Leijnse T. On the modeling of brine transport in porous media. Wat Res Res 1988;24:321–30.
[13] Holzbecher EO. Modeling density-driven flow in porous media. Berlin: Springer; 1998.
[14] Ikeda T. Maximum principle in finite element models for convection–diffusion phenomena. Amsterdam: North-Holland; 1983.
[15] Jianguo H, Shitong X. On the finite volume element method for general self-adjoint elliptic problems. SIAM J Numer Anal 1998;35(5):1762–74.
[16] Johannsen K. Aligned 3D-finite-volumes for convection–diffusion-problems. In: Benkhaldoun F, Vilsmeier R, editors. Finite volumes for complex applications. Paris: Hermes, 1996. p. 291–300.
[17] Knabner P, Frolkovič P. Consistent velocity approximations in finite element and volume discretizations of density driven flow in porous media. In: Aldama AA, et al., editors. Computational methods in water resources XI. Southampton: Computational Mechanics Publications, 1996. p. 93–100.
[18] Knabner P, Tapp C, Thiele K. Adaptive finite volume discretization of density driven flows in porous media. Acta Math Univ Com 1998;67(1):115–36.
[19] Kolditz O, et al. Coupled groundwater flow and transport: 1. Verification of variable density flow and transport models. Adv Wat Res 1998;21(1):27–46.
[20] Konikow LF, Sanford WE, Campbell PJ. Constant-concentration boundary conditions: lessons from the HYDROCOIN variable-density groundwater benchmark problem. Wat Res Res 1997;33(10):2253–61.
[21] Leijnse A. Three-dimensional modeling of coupled flow and transport in porous media, PhD thesis. Indiana: University of Notre Dame, 1992.
[22] Leijnse A, Oostrom M. The onset of instabilities in the numerical simulation of density-driven flow in porous media. In: Peters A, et al., editors. Computational methods in water resources X. Dordrecht: Kluwer Academic Publisher; 1994. p. 489–96.
[23] Oldenburg CM, Pruess K. Dispersive transport dynamics in a strongly coupled groundwater–brine flow system. Wat Res Res 1995;31(4):289–302.
[24] Patankar SV. Numerical heat transfer and fluid flow. New York: Hemisphere; 1980.
[25] Putti M, Paniconi C. Picard and Newton linearization for the coupled model of saltwater intrusion in aquifers. Adv Wat Res 1995;18(3):159–70.
[26] Simmons CT, Narayan KA, Wooding RA. On a test case for density-dependent groundwater flow and solute transport models: the salt lake problem. Wat Res Res 1999;35:3607–20.
[27] Sperb RP. Maximum principles and their applications. New York: Academic Press; 1981.
[28] Trujillo RV. Error analysis of the finite volume element method for elliptic and parabolic partial differential equations, PhD thesis. Denver: University of Colorado; 1996.
[29] van Duijn CJ, Peletier LA, Schotting RJ. Brine transport in porous media: self-similar solutions. Adv Wat Res 1998; 22(3):285–97.
[30] Voss CJ, Souza WR. Variable density flow and solute transport simulation of regional aquifers containing a narrow freshwater–saltwater transition zone. Wat Res Res 1987;23:1851–66.